ADVANCED MATERIALS
www.advmat.de

Ultra-Narrowband Green-Emitting Transparent Composite Ceramics for Laser-Driven Display

Dahai Hu, Shisheng Lin, Tao Pang, Lingwei Zeng, Guoyu Xi, Fengluan You, TianShuo Wu, Xiaoshuang Li,* Bo Wang, Lei Lei, Feng Huang, and Daqin Chen**

Laser-driven projection displays face a critical challenge in developing laser-excitable and high-performance narrowband green emitters. Herein, new Al_2O_3-$LaMgAl_{11}O_{19}$: Mn^{2+} (Al_2O_3-LMA: Mn^{2+}) transparent composite ceramics are reported via high-temperature vacuum sintering, which produces a high-color-purity (95.4%) green emission with full width at half maximum of 24 nm and superior thermal and moisture and laser irradiation stability. These are attributed to low electron-phonon couple, weak crystal-field effect, an individual lattice location of Mn^{2+} activators in high structural rigid host, and the incorporation of a high-thermal-conductivity Al_2O_3 secondary phase. As a result, the composite ceramics are demonstrated as an attractive color converter with a high external quantum efficiency (38%) and absorption coefficient (53%), which ensures a luminous flux of 2012 lm @40.0 W, a luminous efficacy of 67.7 lm W^{-1}, and a green light conversion efficiency of 20.3% upon blue laser irradiation. This enables to construct a brand-new laser-driven prototype display with a record color gamut beyond Rec.2020 standard (100.8%), outperforming commercial YAG: Ce^{3+} and β-SiAlON: Eu^{2+}. This exploration in ultra-narrowband green luminescent materials is poised to accelerate the development of "ideal displays" for laser-driven projection display technology.

1. Introduction

The increasing prevalence of high-quality projection displays in theaters, commercial environments, and educational settings has necessitated the development of new-generation light source technology.[1–4] Traditional display light sources, such as halogen, high-pressure sodium, and mercury lamps, have tended to fall short in terms of system efficiency, color quality, service life, and stability.[5,6] Due to the "efficiency droop" at high incident power density, the widespread light-emitting-diode (LED) is not qualified in high-brightness display applications, and are being supplanted via the emerging laser diode (LD).[4,7] Currently, LD outperforms LED not only in luminescence efficiency at high power but also in ultra-narrowband width, directionality, and system compactness, etc. Nevertheless, the "all laser" approach still encounters serious problems, such as the notorious "green gap" and severe speckle noise.[8] As an alternative, a smart manner is to apply high-power blue LD in combination with down-shifting color converters, which play a vital role in converting blue photons into yellow, green, or red photons. Evidently, laser-driven color converters are crucial to the final display performance.[9–11]

In this context, compared with phosphors in silicone (PiS), single crystal, phosphor in glass (PiG),[12,13] and phosphor-in-glass films (PiGF),[4,14] transparent phosphor ceramic (TPC),[15] with its laser irradiation resistance, superior heat dissipation, and tunable microstructure (pores, secondary phases, or grain

D. Hu, S. Lin, G. Xi, F. You, T. Wu, F. Huang, D. Chen
College of Physics and Energy
Fujian Normal University
Fuzhou, Fujian 350117, P. R. China
E-mail: linshisheng@fjnu.edu.cn; dqchen@fjnu.edu.cn

T. Pang
Huzhou Key Laboratory of Materials for Energy Conversion and Storage
College of Science
Huzhou University
Huzhou, Zhejiang 313000, P. R. China

L. Zeng
School of Chemistry and Chemical Engineering
Hunan University of Science and Technology
Xiangtan, Hunan 411201, P. R. China

The ORCID identification number(s) for the author(s) of this article can be found under https://doi.org/10.1002/adma.202414957

DOI: 10.1002/adma.202414957

X. Li, B. Wang
School of Applied Physics and Materials
Wuyi University
Jiangmen, Guangdong 529020, P. R. China
E-mail: lixiaoshuang12@mails.ucas.ac.cn

L. Lei
Institute of Optoelectronic Materials and Devices
China Jiliang University
Hangzhou, Zhejiang 310018, P. R. China

D. Chen
Fujian Provincial Collaborative Innovation Center for Advanced High-Field Superconducting Materials and Engineering
Fujian Normal University
Fuzhou, Fujian 350117, P. R. China

D. Chen
Fujian Provincial Engineering Technology Research Center of Solar Energy Conversion and Energy Storage
Fujian Normal University
Fuzhou, Fujian 350117, P. R. China

sizes), can be seen as an irreplaceable choice for the laser-driven color converter.[16,17] Currently, the dominant TPCs used for LD-driven displays are commercially available Ce^{3+} doped garnet-structure broadband luminescent materials with full width at half-maximum (FWHM) of ≈100 nm, such as $Y_3Al_5O_{12}$: Ce^{3+} (YAG: Ce^{3+})[18] and $Lu_3Al_5O_{12}$: Ce^{3+} (LuAG: Ce^{3+}),[19] which result in a limited color gamut (≈80%) and significant light loss (≈63%).[20] Therefore, narrowband materials are urgently needed to achieve a wide color gamut display (>100% National Television System Committee (NTSC) standard), but in this regard, especially the lack of narrowband green TPC has not been well addressed, which hinders the development of high-quality LD-driven projection displays.

From the perspective of narrowband color converters, particularly green-emitting ones, although green-emitting quantum dots have ultra-narrow bandwidth (FWHM≈20 nm), either way, the inherent toxic elements, poor stability, and unstable photoluminescence quantum yield caused by surface trap states still restrict their practical application.[21–23] On the other hand, significant endeavors have been employed to fabricate Eu^{2+}-doped green phosphors, such as commercial β-SiAlON: Eu^{2+} (FWHM≈55 nm),[24] $SrGa_2S_4$: Eu^{2+} (FWHM≈47 nm)[25] and UCr_4C_4 oxide-type $RbLi(Li_3SiO_4)_2$: Eu^{2+} (FWHM≈42 nm).[26] Despite their successes, these materials also face challenges due to harsh synthesis conditions and the difficulty of preparing them into inorganic bulk form, which fails to meet the stringent requirements of laser-driven displays (not only high brightness are demanded, but also good resistance to thermal quenching and excellent irradiation robustness should be guaranteed). In pursuit of more cost-effective and reliably preparable color converters, researchers have explored transition-metal Mn^{2+}-based alternatives, such as $ZnAl_2O_4$: Mn^{2+}, Zn_2SiO_4: Mn^{2+} and $Sr_2MgAl_{22}O_{36}$: Mn^{2+} powders.[27–30] Although these materials exhibit remarkable narrowband luminescence characteristics, their development as bulk TPCs is still largely hindered by achieving adequate microstructure densification. Additionally, due to the spin-forbidden *d-d* transitions of Mn^{2+} ions, they always exhibit weak absorption and emission properties. Under such a background, new green-emitting color converters, with facile preparation, ultra-narrow emission band (FWHM ≤ 30 nm), high quantum efficiency, and excellent thermal stability are in urgent demand to overcome the bottleneck of the wide-color-gamut LD-driven displays technique.

Herein, we present a series of Al_2O_3-$LaMgAl_{11}O_{19}$: Mn^{2+} (Al_2O_3-LMA: Mn^{2+}) transparent composite ceramics for the first time. Here, Al_2O_3 serves as both an effective scattering factor and a high-thermal-conductivity counterpart, not only making blue light captured by more LMA but also improving heat dissipation properties. The Al_2O_3-LMA: Mn^{2+} exhibits ultra-narrow green luminescence peaking at 517 nm under 450 nm excitation. The FWHM is only 24 nm, with its color purity reaching an impressive 95.4%, which significantly surpasses that of commercial β-SiAlON: Eu^{2+} (68%). Additionally, the composite exhibits exceptional thermal stability (95.9% at 200 °C) and hydrothermal stability (T_{95} > 1800 h), being superior to the commercial β-SiAlON: Eu^{2+} (91.2% at 200 °C, 92.3% @1800 h). The underlying mechanisms responsible for the narrowband luminescence and exceptional thermal stability were meticulously elucidated. Upon laser irradiation, the optimized Al_2O_3-LMA: Mn^{2+} composite ceramics exhibited remarkable photometric performance, with luminous flux (LF) of 2012 lm @40.0 W, luminous efficiency (LE) of 67.7 lm W^{-1}, green light conversion efficiency of 20.3%, and outstanding laser resistance. Importantly, a brand-new ultra-narrowband ceramics-based projection display system was constructed, achieving a record color gamut of 132.5% NTSC (100.8% Rec.2020, **Table 1**), which is 162% of traditional YAG: Ce^{3+}-based projectors and 122% of commercial β-SiAlON: Eu^{2+}-based projectors.

2. Results and Discussion

Narrowband green-emitting ceramics were synthesized via a high-temperature solid-state reaction under vacuum using oxide/carbonate raw materials (Figure S1, Supporting Information). The LMA: Mn^{2+} TPCs exhibit good transparency and emit intense green light upon blue light excitation (**Figure 1a**; Figure S2, Supporting Information). The fracture surface microstructure of the LMA: Mn^{2+} TPC, examined by scanning electron microscopy (SEM), reveals densely packed grains with randomly distributed bar ranging 50–100 µm, and no secondary phases or impurities at the grain boundaries (Figure 1b). The relative density of 97.5% indicates near-complete densification (Figure S3, Supporting Information). Elemental mapping confirms the homogeneous distribution of La, Mg, Al, O, and Mn within the LMA: Mn^{2+} TPC (Figure S4, Supporting Information). The experimental and calculated XRD profiles as well as their difference converge well (Figure 1c). In Tables S1 and S2 (Supporting Information), the crystallographic parameters and Rietveld refinement results for LMA are summarized. All the diffraction peaks of the as-prepared LMA: $x$$Mn^{2+}$ samples matched well with the standard card data (JCPDS NO. 78–1845),[34] with no impurity phases detected. This indicates the formation of the LMA pure phase. With the increase of Mn^{2+} concentration (Figure S5, Supporting Information), the diffraction peaks progressively shifted to a lower angle side, suggesting the possible substitution of Mg^{2+} ($R_{CN=4}$ = 0.57 Å, CN indicates the coordination number) by Mn^{2+} ($R_{CN=4}$ = 0.66 Å),[34,35] which leads to lattice expansion.

Furthermore, as observed in the photoluminescence excitation (PLE) and transmittance spectra (Figure 1d; Figure S2, Supporting Information), the LMA: Mn^{2+} TPC exhibits strong excitation and absorption bands at 450 nm, matching well with commercial blue LD. Upon 450 nm excitation, LMA: Mn^{2+} TPC demonstrates an ultra-narrowband green emission centered at 517 nm with a FWHM of 24 nm, attributed to the $^4T_1 \rightarrow {}^6A_1$ transition of Mn^{2+} in a highly condensed network structure with a high degree of condensation (κ = 0.68, the molar ratio of (La, Mg, Al):(O), where highly condensed structures require $\kappa \geq 0.5$).[28,36] In contrast, commercial β-SiAlON: Eu^{2+} shows an emission peaking at 540 nm with a FWHM of ≈55 nm under the same excitation wavelength. Compared to standard green light (0.170, 0.797), the LMA: Mn^{2+} TPC exhibits a high color purity of 95.4%, significantly higher than the 68.1% of commercial β-SiAlON: Eu^{2+} (Figure S6, Supporting Information). The narrower FWHM and higher color purity result in higher chromatic saturation of the display image, indicating that LMA: Mn^{2+} TPC is more suitable for wide-color-gamut displays. Figure 1e presents the concentration-dependent photoluminescence (PL)

Table 1. The color gamut of laser-driven displays upon high-power blue laser irradiation and the related optical parameters of color converters.

Laser-driven converter	FWHM [nm]	Thermal behavior [%@200 °C]	Test mode	Luminance Saturation [W·mm^{-2}]	Color gamut [% Rec.2020]	Refs.
$CaAlSiN_3$: Eu^{2+} PiGF @YAG	>105	≈80	static/reflection	7.07	58.6	[7]
$La_3Si_6N_{11}$: Ce^{3+}-$CaAlSiN_3$: Eu^{2+} PiGF @diamond	> 150	≈88	static/reflection	> 40.24	53.3	[4]
β-SiAlON: Eu^{2+} PiGF @sapphire	≈54	≈92	rotation/reflection	> 22	84.3	[14]
β-SiAlON: Eu^{2+}-Calson: Ce^{3+} PiGF @sapphire	≈50	≈86	static/transmission	6.09	81.4	[31]
$CsPbBr_3$ QiG	≈23	≈23 (100 °C)	rotation/reflection	8	95.9	[32]
$CsPbBr_3$-SiO_2 QiGF @sapphire	22	48 (100 °C)	rotation/reflection	4.5	98	[33]
$CsPbBr_3$ QiGF @sapphire	23	–	rotation/reflection	> 20	81.4	[10]
Al_2O_3-LMA: Mn^{2+} TPC	24	95.9	rotation/reflection	> 15.7	100.8	This work

spectra, with the optimum doping content determined to be 0.3, yielding internal quantum efficiency (IQE), absorption efficiency (AE), and external quantum efficiency (EQE) of 60%, 45%, and 27%, respectively (Figure S7, Supporting Information). With the increased Mn content, the emission wavelength and FWHM show no significant difference (Figure 1f), and the fluorescence lifetime monotonously decreases within a small range of 5.82–4.18 ms (Figure S8, Supporting Information), which is attributed to the gradual increased nonradiative transition probability. Considering the inherently forbidden nature of Mn^{2+} *d-d* transitions and the spin-forbidden effects, as well as the significant issue of thermal accumulation under high-power LD irradiation, it is essential to address these challenges for improved laser-driven display performance. In order to mitigate thermal buildup and optimize light extraction efficiency[37] of the developed Mn^{2+}-doped TPCs, the incorporation of a secondary phase, Al_2O_3, was selected.

The introduction of Al_2O_3 is accomplished through precise adjustment in raw material concentrations. In **Figure 2a**, the XRD results indicate that with an increase in Al_2O_3 concentration, the primary LMA phase retains well-defined characteristic diffraction peaks, while the proportion of the secondary phase (Al_2O_3, ICSD No. 9772) increases progressively. Further, the Rietveld refinement results confirm that the addition of Al_2O_3 merely alters the relative content of two phases without producing any impurities or changing the LMA structure (Figure 2b). SEM

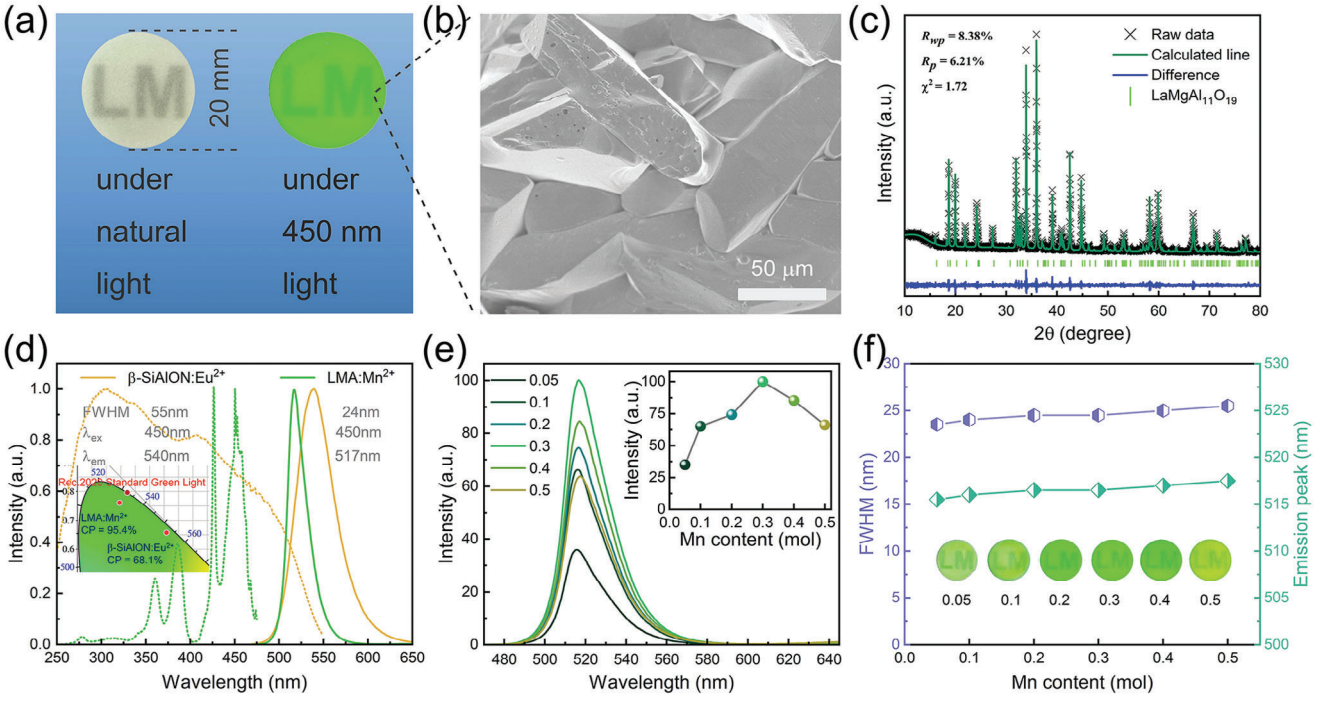

Figure 1. Phase identification, microstructure, and luminescence properties of LMA: Mn^{2+} TPCs. a) The images of LMA: Mn^{2+} TPCs (thickness: 0.45 mm) under natural light and blue light irradiation. b) SEM image of the fracture surfaces of LMA: Mn^{2+} TPCs. c) Rietveld refinement XRD pattern of LMA: Mn^{2+} TPCs. d) PL and PLE spectra of LMA: Mn^{2+} TPCs and commercial β-SiAlON: Eu^{2+} phosphor at room temperature. e) The concentration-dependent PL spectra. The inset shows the corresponding normalized integrated intensity. f) PL peak wavelength and FWHM as a function of Mn^{2+} content. Inset shows appearances of LMA: xMn^{2+} ($0.05 \leq x \leq 0.5$) TPCs (thickness: 0.45 mm) under blue light irradiation.

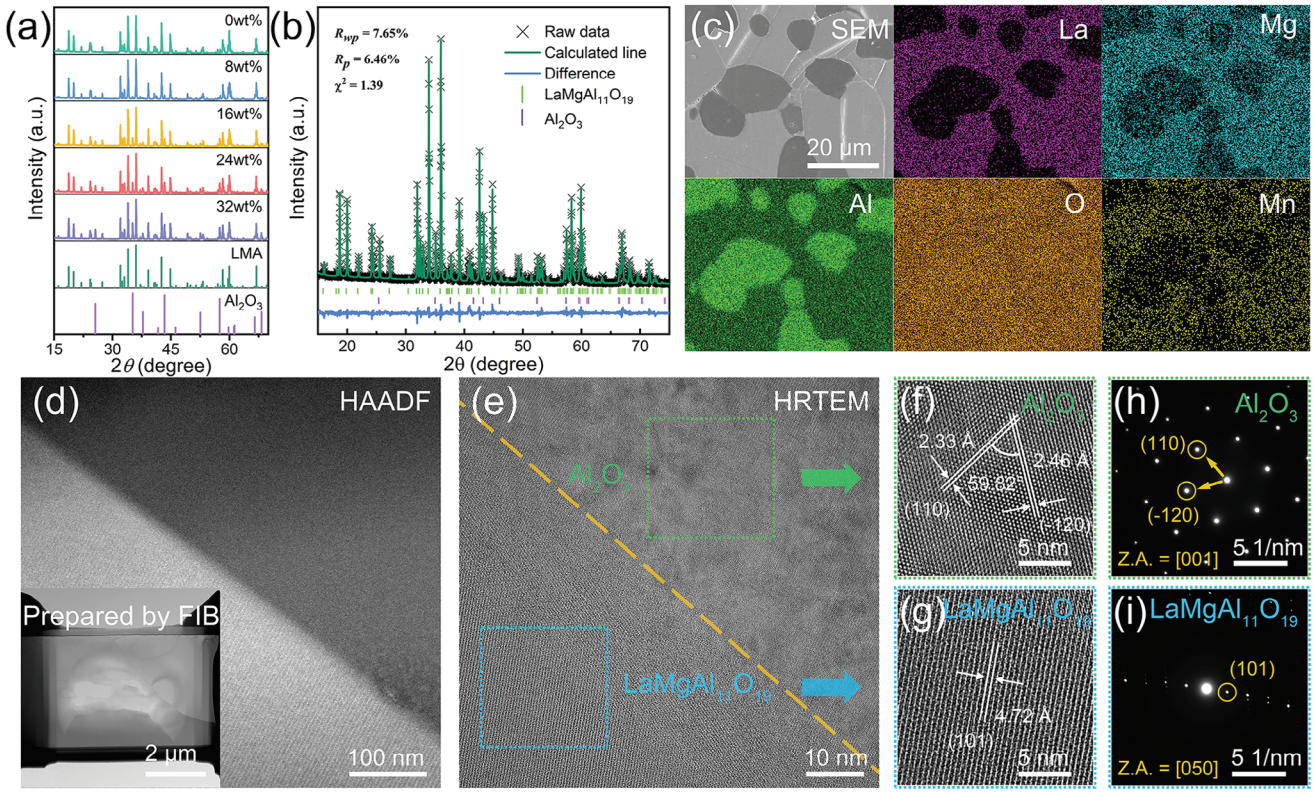

Figure 2. Phase identification and microstructure of Al_2O_3-LMA: Mn^{2+} transparent composite ceramics. a) XRD patterns of Al_2O_3-LMA: Mn^{2+} composite ceramics with different Al_2O_3 concentrations. b) Rietveld refinement pattern of Al_2O_3-LMA: Mn^{2+} composite ceramics. c) SEM and EDS surface mapping to disclose the elemental distributions of La, Mg, Al, O, and Mn of Al_2O_3-LMA: Mn^{2+} composite ceramics. d) HAADF, e-g) HRTEM and h, i) SAED images of interface area of Al_2O_3-LMA: Mn^{2+} composite ceramics.

image and EDS map-scanning analyses of the Al_2O_3-LMA: Mn^{2+} TPC distinctly differentiate the Al_2O_3 particles from the LMA: Mn^{2+} counterpart (Figure 2c), where La-, Mg-, and Mn-rich regions correspond to LMA: Mn^{2+}, while the Al-rich portions are indicative of the Al_2O_3. The elemental mapping images and fluorescence image (Figure S9, Supporting Information) confirm the homogeneous distribution of the Al_2O_3 and LMA: Mn^{2+}, and there is no mutual diffusion of the elements on both sides in the interface region. In order to further investigate the grain boundary between Al_2O_3 and LMA particles, high-angle annular dark-field scanning transmission electron microscopy (HAADF-STEM) was employed on the intergranular boundary of a sample treated with a focused ion beam (FIB) (Figure 2d; Figure S10, Supporting Information). This reveals a stark contrast between LMA: Mn^{2+} (bright) and Al_2O_3 (dark) due to the significant difference in atomic number: La (Z = 57) versus Al (Z = 13). Additionally, a high-resolution TEM (HRTEM) pattern of the interface area presented in Figure 2e and Figure S11 (Supporting Information) shows a clear boundary between the two phases at the nanometer scale. The HRTEM and selected area electron diffraction (SAED) images displays distinct lattice fringes with interplanar spacings of 2.33, 2.46 and 4.72 Å, corresponding to the (110) and (−120) planes of Al_2O_3, and the (101) plane of LMA, respectively (Figure 2f–i). Moreover, the measured angle between (110) and (−120) facets (59.82 °) closely approximate the theoretical value (60 °) of Al_2O_3. Obviously, there is no interfacial reaction at the interfaces (Note S1, Supporting Information). As far as we know, the development of transparent composite ceramics made from $LaMgAl_{11}O_{19}$:Mn^{2+} or Al_2O_3-$LaMgAl_{11}O_{19}$: Mn^{2+} has not reported previously, which dramatically enhances the practical application potential of the material in laser-driven display (Note S2, Supporting Information).

As illustrated in **Figures** 3a and S12 (Supporting Information), the incorporation of Al_2O_3 does not significantly alter the PL peak wavelength, FWHM, and fluorescent lifetime of Al_2O_3-LMA: $0.3Mn^{2+}$, which indicates that the intrinsic luminescence properties of LMA: Mn^{2+} remain unaffected. In the luminescent quantum efficiency measurements, the IQE, blue light AE, and EQE of the transparent composite ceramics initially increased and then sharply decreased with the increased Al_2O_3 content (Figure 3b). The 24 wt.% Al_2O_3-LMA: $0.3Mn^{2+}$ demonstrates an optimal blue light AE of 53%, an IQE of 71%, and an EQE of 38%, attributed to the enhanced converted green light and absorbed blue light from the appropriate scattering effect of Al_2O_3 particles. In this context, multiple scattering extends the propagation path of incident blue light within the composite ceramics (evidenced by decreased transmittance),[37] thus improving the conversion efficiency to green light (Figures S13 and S14, Supporting Information). Although ceramics indeed have tunable microstructure features (such as pores, secondary phases, and grain sizes), and relevant prior research can be a useful foundation, this does not diminish the innovation of this work (Note S3,

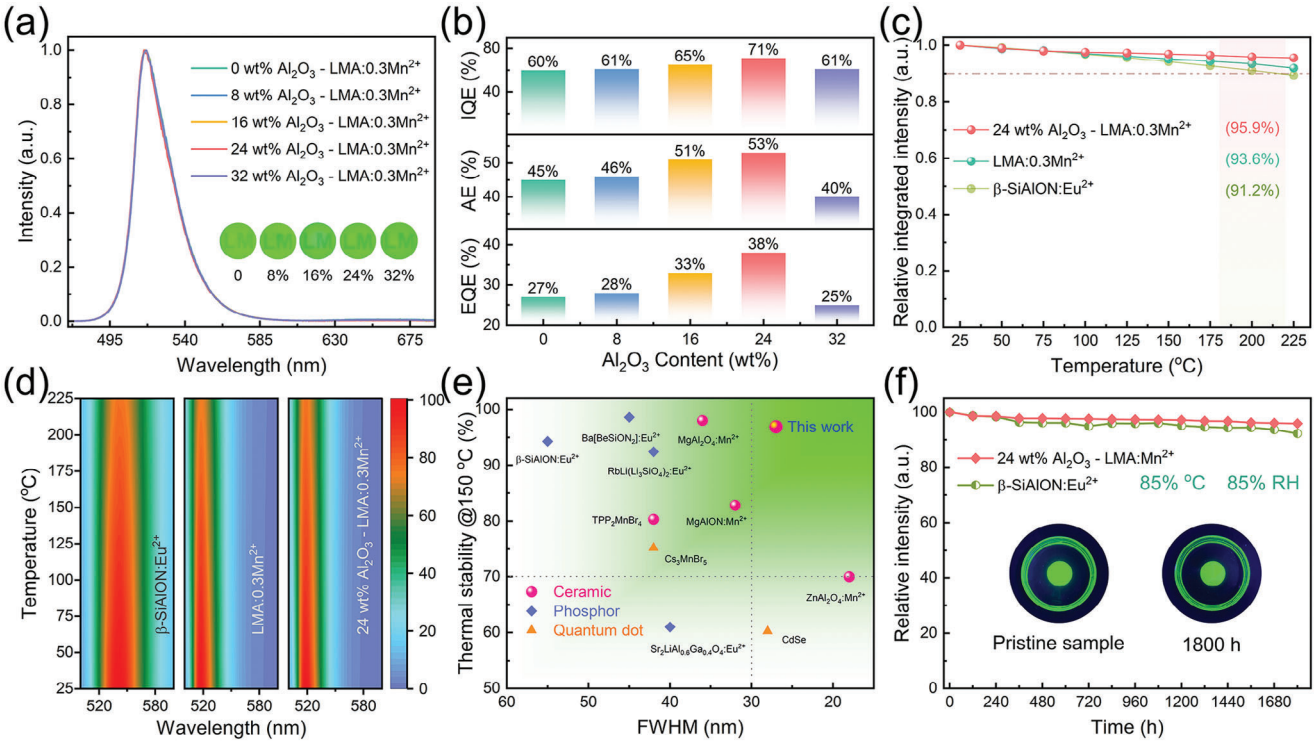

Figure 3. Luminous performance and stability of Al2O3-LMA: Mn^{2+} transparent composite ceramics. a) Normalized PL spectra of yAl_2O_3-LMA: 0.3Mn^{2+} ($0 \leq y \leq 32$ wt.%) composite ceramics. Inset shows the appearance of Al_2O_3-LMA: Mn^{2+} composite ceramics (thickness: 0.45 mm) under blue light irradiation. b) The IQE, AE, and EQE of Al_2O_3-LMA: Mn^{2+} composite ceramics. c) Temperature-dependent normalized intensities and d) 2D-contour plot of temperature-dependent PL spectra of 24 wt.%Al_2O_3-LMA: 0.3Mn^{2+} composite ceramics, LMA: 0.3Mn^{2+} TPC and β-SiAlON: Eu^{2+} phosphor. e) Summary of the reported narrowband green materials on the basis of FWHM and thermal stability. f) Stability test of 24 wt.%Al_2O_3-LMA: 0.3Mn^{2+} composite ceramics and β-SiAlON: Eu^{2+} phosphor under accelerated aging condition at 85 °C/85% RH. Insets show photographs of the 24 wt.%Al_2O_3-LMA: 0.3Mn^{2+} composite ceramics before and after treatment.

Supporting Information). However, when the amount of Al_2O_3 exceeded 32 wt.%, the dilution effect predominated, resulting in a reduced concentration of LMA: Mn^{2+} per unit volume and a subsequent decline in quantum efficiency. Notably, although the luminescent quantum efficiency is slightly lower than that of β-SiAlON: Eu^{2+} (88.4%, Figure S15, Supporting Information), due to the transparency of the developed composite ceramics, it exhibits a luminous flux (LF) of 244.8 lm under blue laser excitation (6W), which is higher than that of β-SiAlON: Eu^{2+} (213.7 lm, Figure S16, Supporting Information).

Thermal stability is crucial for color converters in practical device applications. The temperature-dependent PL properties of 24 wt.%Al_2O_3-LMA: 0.3Mn^{2+}, LMA: 0.3Mn^{2+}, and commercial β-SiAlON: Eu^{2+} were investigated under 450 nm excitation within the temperature range of 25–225 °C (Figure 3c,d; Figure S17, Supporting Information). At 200 °C, the luminescent losses of 24 wt.%Al_2O_3-LMA: 0.3Mn^{2+}, LMA: 0.3Mn^{2+}, and β-SiAlON: Eu^{2+} were 4.1%, 6.4% and 8.8%, respectively. Intriguingly, as the temperature increased from 25 to 225 °C, the FWHM of emission spectrum of Al_2O_3-LMA: Mn^{2+} composite ceramic was only slightly broadened, ranging 24–28 nm, because of more excited electrons spreading to the higher vibration levels before returning to the ground state via radiative transition, which is more stable than the 55–65 nm range observed in β-SiAlON: Eu^{2+} (Figure S17, Supporting Information). These results indicate that the ultra-narrowband green emission characteristics of Al_2O_3-LMA: Mn^{2+} transparent composite ceramics can be maintained even at high working temperatures. Thermoluminescence measurements were conducted to investigate the mechanism of robust thermal-quenching behavior, revealing the absence of defect-related carrier trapping in the sample (Figure S18, Supporting Information). The LMA belongs to the hexagonal P63/mmc space group,[34,35] characterized by a high-symmetry framework consisting of [Mg/AlO_4] tetrahedra and [AlO_6] octahedra interconnected through corner-sharing (Figure S19, Supporting Information), which could minimize the structural relaxation of the luminescent center in the excited state; meanwhile, the Mg sites are isolated and spaced at a considerable distance (d = 5.58 Å), which further reduces energy transfer and interactions between Mn^{2+} ions. On the other hand, as depicted in Figure S20 (Supporting Information), the thermal conductivity of the LMA: Mn^{2+} and Al_2O_3-LMA: Mn^{2+} samples are measured to be 2.2 and 12.8 W $m^{-1}K^{-1}$, respectively. Evidently, the incorporation of the secondary phase Al_2O_3 (exhibiting a high thermal conductivity of 32–35 W $m^{-1}K^{-1}$)[18] significantly enhanced the overall thermal conductivity (increased by 581%), reaching 12.8 W $m^{-1}K^{-1}$ for 24 wt.% Al_2O_3-LMA: Mn^{2+} composite ceramic. This improvement facilitates rapid dissipation of accumulated heat even at elevated temperatures, ensuring that the temperature at the laser irradiation point remains

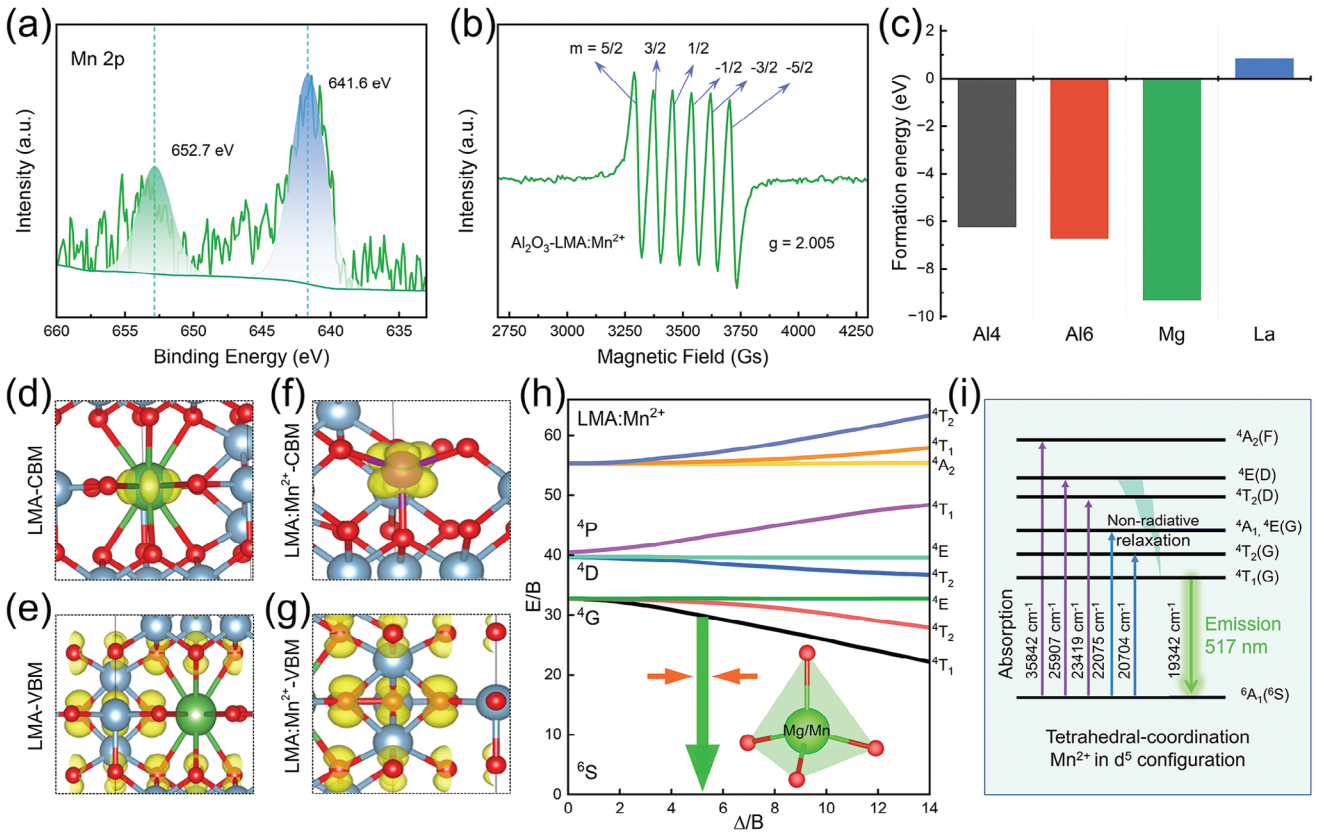

Figure 4. Local environments and electronic structure of Al_2O_3-LMA: Mn^{2+}. a) high-resolution XPS profile at Mn 2p position and b) EPR spectrum of Al_2O_3-LMA: Mn^{2+} transparent composite ceramics. c) The dopant formation energies of Mn^{2+} substituting the sites in LMA models. CBM-and VBM-associated charge densities for d,e) LMA and f,g) LMA: Mn^{2+} (Green ball: La, Orange ball: Mg, Gray ball: Al, Red ball: O, Purple ball: Mn). h) Tanabe-Sugano energy-level diagram of Mn^{2+} in the LMA host. i) Schematic of the energy diagram of Mn^{2+} transition processes.

low to effectively mitigate thermal quenching. As illustrated in Figure 3e, the Al_2O_3-LMA: Mn^{2+} transparent composite ceramics demonstrate exceptional performance advantages over currently reported green-emitting materials,[21,24,26,28,38–40] encompassing phosphors, quantum dots, luminescent ceramics, and commercial phosphors.

Moreover, the Al_2O_3-LMA: Mn^{2+} transparent composite ceramics demonstrate remarkable resistance to aging. In an accelerated aging test lasting over 1800 h at 85 °C/85% RH, the PL intensities of Al_2O_3-LMA:Mn^{2+} composite ceramic retained over 95.8% of its initial value (Figure 3f; Figure S21, Supporting Information), which surpasses the stringent commercial operational lifetime standard (T_{90} > 1040 h; T_{90} is the time required for the material's PL intensity to maintain 90% of its initial one after stability testing)[41] and is superior to commercial β-SiAlON: Eu^{2+} phosphor (92.3% @1800 h). The outstanding aging resistance renders developed transparent composite ceramics an ideal candidate for deployment in extremely harsh application environments. Evidently, Al_2O_3-LMA: Mn^{2+} transparent composite ceramics stand out as the leading candidate for narrowband green-emitting materials, ensuring the most comprehensive performance and suitability for practical applications.

In order to elucidate the valence state of manganese in Al_2O_3-LMA: Mn^{2+} transparent composite ceramics, an X-ray photoelectron spectroscopy (XPS) analysis was conducted (Figure S22, Supporting Information). **Figure** 4a presents the high-resolution XPS profile of the Mn 2p orbital in the synthesized Al_2O_3-LMA: Mn^{2+} composite ceramics. The two prominent XPS peaks of 641.6 and 652.7 eV correspond to the Mn^{2+} $^2p_{3/2}$ and $^2p_{1/2}$ states, respectively, confirming manganese's divalent state.[28] Typically, three Kramers doublets (±5/2, ±3/2, and ±1/2) emerge when octahedral or tetrahedral symmetry sites occupied by d^5 transition metal ions undergo axial distortion.[42] Figure 4b displays the electron paramagnetic resonance (EPR) spectrum of LMA: $0.3Mn^{2+}$ composite ceramics at room-temperature, revealing a clearly discernible sextet of hyperfine peaks due to the interaction between unpaired electrons and the 55Mn nucleus (nuclear spin quantum number I = 5/2). The g factor is ≈2.005, indicating that Mn behaves as a bivalent state.[42]

Additionally, the formation energies of Mn substitutions at various lattice sites were calculated to better understand the substitutional behavior of Mn in the host lattice by considering crystal symmetry and defect chemistry. According to the results, Mn is the most energetically favorable to substitute at the Mg site, exhibiting the lowest formation energy among the considered sites (Figure 4c). Evidently, only one crystallographic dopant site is advantageous for Mn^{2+} to achieve ultra-narrowband emission. Moreover, the host material exhibits a bandgap of 4.10 eV (Figure S23, Supporting Information), matching the experimental value

of 4.25 eV (Figure S2, Supporting Information). The conduction band minimum (CBM) is primarily derived from La elements, while the valence band maximum (VBM) is predominantly occupied by O atoms. Upon substituting Mn at the Mg site, the recalculated electronic structure reveals a substantial reduction in the bandgap to 3.21 eV (Figure S23, Supporting Information). In this doped configuration, the CBM is primarily composed of Mn states, leading to the introduction of impurity levels within the bandgap. Further, notable changes in electronic properties were observed due to Mn doping (Figure 4d–g; Figure S24, Supporting Information). Given that Mn^{2+} possesses lower electronegativity than Mg^{2+}, the incorporation of Mn into the lattice induces electron transfer to the adjacent O atoms, thus distorting the electric field environment surrounding the Mg/Mn centers. This electron redistribution substantially modifies the local electronic environment, contributing to the observed bandgap reduction. Evidently, the presence of Mn^{2+} notably influences key properties, including energy band structure, state density, and differential charge distribution of LMA. As illustrated in Figures S19 and S25 (Supporting Information), the LMA structure contains a single Mg/Mn site ([Mg/MnO_4] tetrahedron) with an extended average bond length of 1.942 Å and a minimal distortion index of 0.01 (calculated using Equation S9, Supporting Information), suggesting that the Mn-doped sites exhibit high coordination symmetry and weak crystal field. According to the Tanabe-Sugano diagram[43] (Figure 4h), it can be seen that under the influence of the weak crystal field, the photoluminescence spectrum experiences minimal broadening. By fitting the relationship between FWHM and temperature,[44,45] the Huang-Rhys factor (S) that reflects electron–phonon coupling was determined to be 1.24, whose low value indicates weak electron–phonon interaction (Equation S10 and Figure S26, Supporting Information). Consequently, due to the individual lattice location, weak crystal field, and low electron–phonon interaction, a narrow green emission, corresponding to the spin-and parity-forbidden *d-d* ($^4T_1 \rightarrow {}^6A_1$) transition, was successfully achieved in Al_2O_3-LMA: Mn^{2+} transparent composite ceramics (Figure 4i).

The luminescent properties of Al_2O_3-LMA: Mn^{2+} transparent composite ceramics under blue laser irradiation were studied using a self-built platform consisting of a 450 nm blue laser, integrating sphere, fiber spectrometer, laser power meter, and infrared thermal imaging camera (Figure S27, Supporting Information). In order to address the luminescence saturation observed under low-power excitation in static mode (Figure S28, Supporting Information), the Al_2O_3-LMA: Mn^{2+} composite ceramic was fabricated into a rotating wheel, a common technique used in laser-driven projection display/lighting.[46,47] The color-conversion wheel, mounted on a micro-motor rotating at 3000 rpm, exhibited no luminescence saturation even when the input blue laser power (P_{in}) was increased to the maximum limit of 40.0 W (15.7 W mm^{-2}), achieving an impressive maximum luminous flux (LF) 2012 lm @40.0 W (15.7 W mm^{-2}), a high luminescence efficiency (LE) of 67.7 lm W^{-1}, and a substantial converted green light power (**Figure 5**a,b; Figure S29, Supporting Information). Evidently, the luminous performance of the developed composite reported in this study can meet the requirements of laser-driven displays (Note S4, Supporting Information). As shown in Figure 5c, the green light conversion efficiency reached the maximum value of 20.3% for 24 wt.% Al_2O_3-LMA: 0.3Mn^{2+}, while the chromaticity coordinates remained stable with deviations less than 0.01 as P_{in} increased (Figure 5d). The difference between the results of conversion efficiency and IQE is mainly ascribed to the different excitation sources used, with the former one of the high-power-density blue laser and the latter one of the non-coherent Xenon lamps. The blue laser excitation undoubtedly induces more severe thermal elevation and thus accelerates the non-radiative transitions of Mn^{2+} to produce lower conversion efficiency.

Simultaneously, thermal infrared images reveal a rapid increase in the surface temperature of the sample in static mode, reaching up to 364.5 °C @10.0 W (3.9 W mm^{-2}) (Figure S28, Supporting Information). However, in the rotating mode, the surface temperature of the Al_2O_3-LMA: Mn^{2+} composite ceramic wheel reached only 79.3 °C under 40.0 W (15.7 W mm^{-2}) blue laser irradiation (Figure 5e). The rotation not only converts continuous excitation into pulsed excitation, reducing optical saturation but also facilitates heat dissipation, mitigating thermal accumulation and preventing thermal saturation. Notably, the Al_2O_3-LMA: Mn^{2+} transparent composite ceramics demonstrate exceptional luminescence stability, with no degradation in green emission intensity after continuous operation for 120 min under 40.0 W 450 nm blue LD irradiation (Figure 5f).

The ultra-narrowband green emission, combined with exceptional thermal, environmental, and LD irradiation stability, positions Al_2O_3-LMA: Mn^{2+} composite ceramics as an excellent candidate for wide-color gamut laser-driven displays. In order to facilitate comparison, prototype projection displays were constructed by using YAG: Ce^{3+} TPC, β-SiAlON: Eu^{2+} PiGF, and Al_2O_3-LMA: Mn^{2+} TPC, incorporating blue/red LDs, corresponding color converters wheels, RGB color filters, liquid crystal display (LCD) module, dichroic filters, and various lens groups (**Figure 6**a). In the YAG TPC-based system, blue LD is combined with broadband-emission YAG, necessitating the filtering of the broad-spectrum light to produce the R/G/B primary colors. In contrast, both β-SiAlON: Eu^{2+} PiGF and Al_2O_3-LMA: Mn^{2+} TPC directly emits narrowband blue, green, and red light (Figure 6b–d). Consequently, as shown in the display images (Figure 6e–g), the YAG: Ce^{3+} TPC-based system demonstrates the lowest color saturation, particularly in the green region, resulting in a yellowish-green hue. In comparison, the Al_2O_3-LMA: Mn^{2+} TPC-based demo delivers a more vibrant and realistic green, with significantly higher saturation than the well-regarded β-SiAlON: Eu^{2+} PiGF-based display. Correspondingly, the Al_2O_3-LMA: Mn^{2+} TPC-based laser-driven projection display system achieved an exceptionally wide color gamut, covering 132.5% NTSC (100.8% Rec.2020), far surpassing both the YAG TPC-based system (62.1% Rec.2020) and the β-SiAlON: Eu^{2+}-based system (82.8% Rec.2020) (Figure 6h; Table S3, Supporting Information), even representing the widest gamut reported to date (Table 1). This work makes Mn^{2+}-activated narrowband-emitting materials take a key step toward practical application (Note S5, Supporting Information).

3. Conclusion

In summary, ultra-narrowband green-emitting Al_2O_3-LMA: Mn^{2+} transparent composite ceramics were synthesized for the first time, featuring an emission peak at 517 nm, with a FWHM

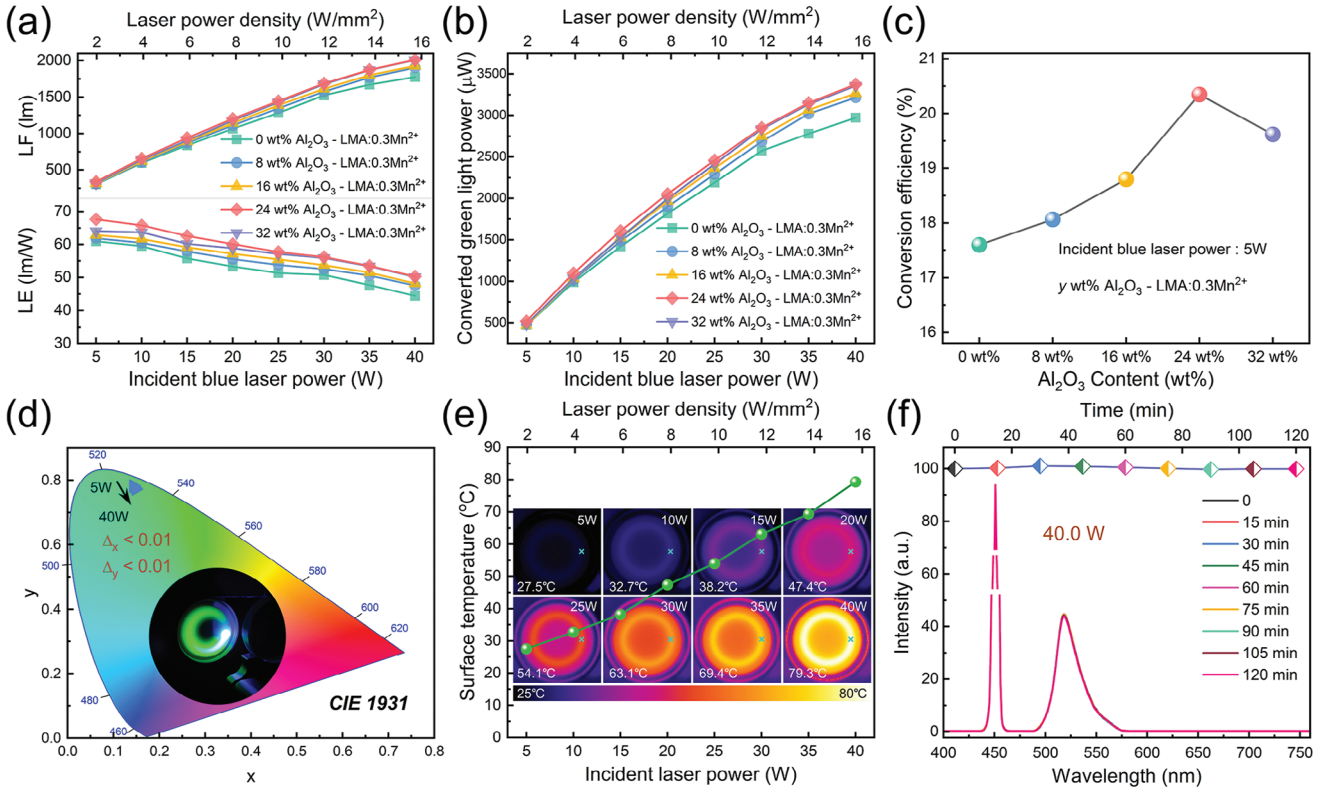

Figure 5. The optical performance of Al2O3-LMA: Mn^{2+} transparent composite ceramics under blue laser excitation. a) Pin-dependent LF, LE, b) converted green light power, c) conversion efficiency, and d) CIE chromaticity coordinates change in rotation mode. Inset of d) shows the photograph of the rotated "ceramic wheel" under 450 nm laser irradiation. e) Thermal infrared images and local temperature at the laser spot of the 24 wt.%Al_2O_3-LMA: 0.3Mn^{2+} composite ceramics in rotation mode after 5 min of blue laser irradiation with different powers. f) Electroluminescent (EL) spectra and normalized integrated intensity variation upon 40.0 W (15.7 W·mm^{-2}) blue laser irradiation for 120 min.

of 24 nm and a color purity of 95.4%. These composites exhibit outstanding thermal/hydrothermal stability and robust laser resistance, making them ideal for laser-driven display applications. The narrowband emission ($^4T_1 \rightarrow {}^6A_1$) results from low electron-phonon interaction, weak crystal field, and individual lattice location. Meanwhile, their exceptional thermal stability is attributed to the rigid crystal structure, the isolated luminescence center within the [Mg/MnO_4] tetrahedral site, and the incorporation of Al_2O_3 phase (enhancing thermal conductivity to 12.8 W·m^{-1}K^{-1}). Under laser irradiation, the optimized ceramic demonstrates impressive LF of 2012 lm @40.0 W, LE of 67.7 lm W^{-1}, and green light conversion efficiency of 20.3%. Ultimately, the laser-driven projection display prototype constructed by using the developed composite ceramic can achieve a color gamut of 100.8% Rec.2020, which surpasses that of YAG: Ce^{3+}-based and β-SiAlON: Eu^{2+}-based prototypes. The outcomes of this research represent obvious progress, laying a significative foundation for the future development of state-of-the-art and wide-color-gamut laser-driven projection display technology.

4. Experimental Section

Material Preparation: A series of yAl_2O_3-$LaMgAl_{11}O_{19}$: xMn^{2+} ($0.05 \le x \le 0.5$, $0 \le y \le 32$ wt.%) transparent composite ceramics were synthesized via a vacuum sintering technique, where the used raw materials were Al_2O_3 (TM-DAR, Tokyo, Japan, 99.99%), La_2O_3 (Innochem Corporation, Beijing, China, 99.99%), MgO (Innochem Corporation, Beijing, China, 99.99%), and $MnCO_3$ (Innochem Corporation, Beijing, China, 99.99%). The precursor powders were accurately weighed and subsequently ball-milled in ethanol at 250 rpm for 24 h. After that, the slurry was dried at 80 °C for 6 h and sieved using a 200-mesh screen. The mixtures were then calcined in air at 600 °C for 24 h to eliminate impurities. The resulting green bodies were pressed into shape using a stainless-steel mold ($\Phi = 20$ mm) under an axial load of 20 MPa, followed by cold isostatic pressing (CIP) at 260 MPa for 20 min. The pressed green bodies underwent additional calcination at 850 °C for 24 h in air to remove any remaining organic residues. Final sintering was performed in a vacuum furnace (Nanjing Boyuntong Instrument Co., Ltd., China) with a vacuum pressure of 5×10^{-4} Pa at 1850 °C for 8 h. The samples were annealed in air at 800 °C for 4 h. Upon cooling, both sides of the samples were polished for subsequent characterization.

Characterization: The microstructural analyses were carried out using a JEOL JEM-2010 transmission electron microscopy, equipped with a high-resolution transmission electron microscope (HR-TEM), energy dispersive X-ray (EDX) mapping, and high-angle annular dark-field (HAADF) STEM, all operating at an acceleration voltage of 200 kV. Cross-sectional and surface morphologies of the Al_2O_3-LMA: Mn^{2+} composite ceramics were examined via scanning electron microscopy (SEM, COXEM EM-30) coupled with energy dispersive spectroscopy (EDS) (Hitachi SU8220). Phase purity and crystallographic structure were analyzed using an X-ray polycrystalline powder diffractometer (SmartLab Rigaku) with Cu Kα radiation (λ = 0.154 nm), operating at 40 kV and 30 mA, and scanning at a rate of 5 min^{-1} over a 2θ range of 10°–80°.

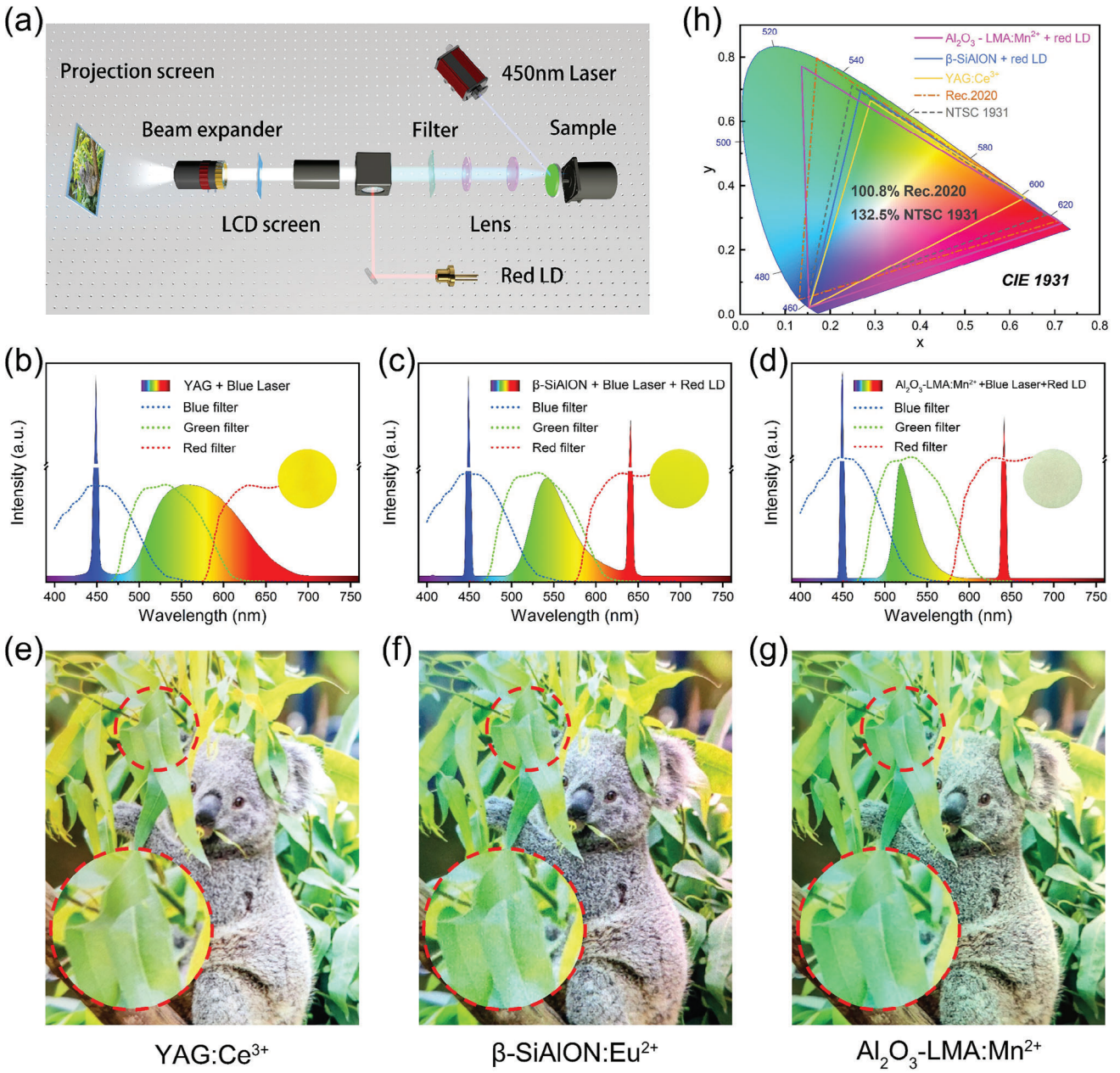

Figure 6. Construction of laser-driven wide-color-gamut display. a) Illustration of the light path for the Al2O3-LMA: Mn^{2+}-based laser-driven projection system. EL spectra of b) commercial YAG: Ce^{3+} TPC, c) β-SiAlON: Eu^{2+} PiGF, and d) Al_2O_3-LMA: Mn^{2+} composite ceramics -based laser-driven projector prototypes. e-g) The actual display performance and h) the corresponding color gamut of the three different kinds of projections.

Photoluminescence emission (PL), photoluminescence excitation (PLE), decay curves, and photoluminescence quantum yield (PLQY) were measured using a fluorescence spectrometer (FLS1000, Edinburgh Instruments, UK) equipped with a 450 W continuous xenon lamp. Temperature-dependent PL spectra were also obtained with this spectrometer, using a heating attachment (THMS600E, Linkam Scientific Instruments). The samples were heated to 225 in 25 °C intervals at a rate of 50 °C min^{-1}, with a 5 min holding period at each temperature to achieve thermal equilibrium. Photometric and colorimetric parameters under blue laser excitation were recorded using a custom-built laser illumination system comprising an integrating sphere (30 cm in diameter, Labsphere, Inc., USA), a blue laser source (LSR-PS-FA, Lasever, China), and a CCD spectrometer (OHSP-350 M, Hopoocolor Technology Co., Ltd., China) operating in reflection mode. The laser spot size was adjusted to a 2.543 mm^2 area using a lens. Thermographic imaging under varying blue laser diode (LD) power densities was captured using an infrared thermal camera (TiS75, Fluke, USA), positioned 15 cm from the sample.

The thermal diffusivity of the ceramic was determined using a laser flash apparatus (LFA 467, Netzsch). X-ray photoelectron spectroscopy (XPS) was performed on a Thermo Scientific K-Alpha (Thermo Scientific Inc., USA) using a monochromatic Al Kα source. Additionally, electron paramagnetic resonance (EPR) spectra were measured at room-temperature with an EMXplus X-band spectrometer (Bruker).

Computational Procedure: Utilizing density functional theory (DFT) as implemented in the Vienna *ab-initio* simulation package code,[48] the electronic structures of LMA were investigated. The projector augmented wave (PAW) method[49] was used for the ionic cores and the generalized gradient approximation (GGA) for the exchange-correlation potential, in which the Perdew-Burke-Ernzerhof (PBE) type[50] exchange-correlation was adopted. The reciprocal space was sampled with 0.03 $Å^{-1}$ spacing in the Monkhorst-Pack scheme for structure optimization, while denser k-point grids with 0.01 $Å^{-1}$ spacing were adopted for properties calculation. A mesh cutoff energy of 400 eV was used to determine the self-consistent charge density. All geometries were relaxed until the Hellmann–Feynman force on atoms is less than 0.01 eV $Å^{-1}$ and the total energy change is less than 1.0×10^{-5} eV. The calculation models were built from the crystal structure.

Supporting Information

Supporting Information is available from the Wiley Online Library or from the author.

Acknowledgements

This research was supported by the National Natural Science Foundation of China (12304442, 52272141, 51972060, 12074068, 52102159, and 22103013), and the Natural Science Foundation of Fujian Province (2024J02014, 2022J05091, 2021J06021, and 2021J01190).

Conflict of Interest

The authors declare no conflict of interest.

Author Contributions

S.S.L. conceived the composite ceramic design. D.H.H. synthesized the material and wrote the first draft. S.S.L. and D.Q.C. helped D.H.H. to analyze the experimental results and finish the final manuscript. T.P., L.W.Z., L.L., and F.H. provided constructive suggestions for data analyses. G.Y.X., F.L.Y., and T.S.W. helped to measure the spectroscopy. X.S.L. and B.W. helped to make a computational procedure. D.Q.C. supervised the project.

Data Availability Statement

The data that support the findings of this study are available from the corresponding author upon reasonable request.

Keywords

laser-driven projection displays, luminescent materials, narrowband emitters, transparent ceramics

Received: October 1, 2024
Revised: November 26, 2024
Published online:

[1] J. Li, P. Yu, S. Zhang, N. Liu, *Nat. Commun.* **2020**, *11*, 3574.
[2] T. Kim, K-H. Kim, S. Kim, S-M. Choi, H. Jang, H-K. Seo, H. Lee, D.-Y. Chung, E. Jang, *Nature* **2020**, *586*, 385.
[3] T. Xuan, S. Guo, W. Bai, T. Zhou, L. e. Wang, R-J. Xie, *Nano Energy* **2022**, *95*, 107003.
[4] Z. Yu, J. Zhao, Z. Yang, Y. Mou, H. Zhang, R. Xu, Q. Wang, L. Zeng, L. Lei, S. Lin, H. Li, Y. Peng, D. Chen, M. Chen, *Adv. Mater.* **2024**, *36*, 2406147..
[5] E. F. Schubert, J. K. Kim, *Science* **2005**, *308*, 1274.
[6] M. A. Triana, E.-L. Hsiang, C. Zhang, Y. Dong, S. T. Wu, *ACS Energy Lett.* **2022**, *7*, 1001.
[7] S. Liao, S. Jin, T. Pang, S. Lin, Y. Zheng, R. Chen, G. Xi, X. Li, B. Zhuang, F. Huang, D. Chen, *Adv. Funct. Mater.* **2024**, *34*, 2307761.
[8] S. Pleasants, *Nat. Photonics* **2013**, *7*, 585.
[9] S. Li, L. Wang, N. Hirosaki, R.-J. Xie, *Laser Photonics Rev.* **2018**, *12*, 1800173.
[10] S. Liao, Z. Yang, J. Lin, S. Wang, J. Zhu, S. Chen, F. Huang, Y. Zheng, D. Chen, *Adv. Funct. Mater.* **2023**, *33*, 2210558.
[11] J. Liu, Y. Zhu, T. Tsuboi, C. Deng, W. Lou, D. Wang, T. Liu, Q. Zhang, *Nat. Commun.* **2022**, *13*, 4876.
[12] D. Zhang, W. Xiao, C. Liu, X. Liu, J. Ren, B. Xu, J. Qiu, *Nat. Commun.* **2020**, *11*, 2805.
[13] C. Liu, W-T. Huang, J. Li, Y. u.-C. Lee, T-L. Tsai, F-C. Shen, W-W. Wu, R. u.-S. Liu, X. Zhang, *Adv. Opt. Mater.* **2023**, *11*, 2300963.
[14] X. Yue, J. u. Xu, H. Lin, S. Lin, R. Li, B. o. Wang, Q. Huang, P. Wang, P. Sui, Y. Cheng, Y. Wang, *Laser Photonics Rev.* **2021**, *15*, 2100317.
[15] Q. i. Yao, P. Hu, P. Sun, M. Liu, R. Dong, K. Chao, Y. Liu, J. Jiang, H. Jiang, *Adv. Mater.* **2020**, *32*, 1907888.
[16] Y. Sun, Y. Wang, W. Chen, Q. Jiang, D. Chen, G. Dong, Z. Xia, *Nat. Commun.* **2024**, *15*, 1033.
[17] Z. Cheng, X. Liu, X. Chen, J. Xu, Y. Wang, T. Xie, L. Wu, Z. Dai, G. Zhou, J. Zou, J. Li, *J. Adv. Ceram.* **2023**, *12*, 625.
[18] G. Xi, Z. Zhou, J. Li, L. Zeng, S. Lin, P. Wang, H. Lin, Y. Wang, S. u. Zhou, F. Huang, G. Chen, D. Chen, *Adv. Funct. Mater.* **2024**, *34*, 2401026.
[19] H. Ding, Z. Liu, P. Hu, Y. Liu, P. Sun, Z. Luo, X. Chen, H. Jiang, J. Jiang, *Adv. Opt. Mater.* **2021**, *9*, 2002141.
[20] F. Hu, C. Zhang, Z. Guo, C. Chen, Y. Li, *SID Int. Symp. Dig. Tech. Pap.* **2020**, *51*, 1234.
[21] S. Li, Y. Pan, W. Wang, Y. Li, *Chem. Eng. J.* **2022**, *434*, 134593.
[22] H. Tang, Y. Xu, X. Hu, Q. Hu, T. Chen, W. Jiang, L. Wang, W. Jiang, *Adv. Sci.* **2021**, *8*, 2004118.
[23] Z. e. Yang, H. Zhang, Z. Fang, J. Yi, P. Song, X. Yu, D. Zhou, J. Qiu, X. Xu, *Chem. Eng. J.* **2022**, *427*, 131379.
[24] S. Li, L. e. Wang, D. Tang, Y. Cho, X. Liu, X. Zhou, L. u. Lu, L. Zhang, T. Takeda, N. Hirosaki, R-J. Xie, *Chem. Mater.* **2018**, *30*, 494.
[25] M. Zhao, Q. Zhang, Z. Xia, *Mater. Today* **2020**, *40*, 246.
[26] M. Zhao, H. Liao, L. Ning, Q. Zhang, Q. Liu, Z. Xia, *Adv. Mater.* **2018**, *30*, 1802489.
[27] C. Bertail, S. Maron, V. Buissette, T. Le Mercier, T. Gacoin, J-P. Boilot, *Chem. Mater.* **2011**, *23*, 2961.
[28] E. H. Song, Y. Y. Zhou, Y. Wei, X. X. Han, Z. R. Tao, R. L. Qiu, Z. G. Xia, Q. Y. Zhang, *J. Mater. Chem. C.* **2019**, *7*, 8192.
[29] Y. Zhu, Y. Liang, S. Liu, H. Li, J. Chen, *Adv. Opt. Mater.* **2019**, *7*, 1801419.
[30] L. Zheng, L. Zhang, L. Fang, H. Wu, H. Wu, G-H. Pan, Y. Yang, Y. Luo, Z. Hao, J. Zhang, *Adv. Opt. Mater.* **2024**, *12*, 2301480.
[31] L. e. Wang, R. Wei, P. Zheng, S. You, T-L. Zhou, W. Yi, T. Takeda, N. Hirosaki, R-J. Xie, *J. Mater. Chem. C* **2020**, *8*, 1746.
[32] S. Lin, H. Lin, G. Chen, B. o. Wang, X. Yue, Q. Huang, J. u. Xu, Y. Cheng, Y. Wang, *Laser Photonics Rev.* **2021**, *15*, 2100044.
[33] J. Sun, Z. Lu, Y. i. Liu, D. Zheng, J. Li, L. Jin, J. Zhang, H. Zhang, Y. Liu, X. Zhang, B. Lei, *J. Mater. Chem. C.* **2022**, *10*, 17109.
[34] C. Zhan, H. Zhu, S. Liang, Y. Huang, W. Nie, Z. Wang, M. Hong, *J. Mater. Chem. C.* **2024**, *12*, 6932.
[35] Z. Wu, C. Li, F. Zhang, S. Huang, F. Wang, X. Wang, H. Jiao, *J. Mater. Chem. C.* **2022**, *10*, 7443.

[36] P. Strobel, C. Maak, V. Weiler, P. J. Schmidt, W. Schnick, *Angew. Chem., Int. Ed.* **2018**, *57*, 8739.
[37] J. Wang, X. Tang, P. Zheng, S. Li, T. Zhou, R-J. Xie, *J. Mater. Chem. C.* **2019**, *7*, 3901.
[38] K. Han, J. Jin, X. Zhou, Y. Duan, M. V. Kovalenko, Z. Xia, *Adv. Mater.* **2024**, *36*, 2313247.
[39] T. Giftthaler, P. Strobel, V. Weiler, A. Haffner, A. Neuer, J. Steinadler, T. Bräuniger, S. D. Kloß, S. Rudel, P. J. Schmidt, W. Schnick, *Adv. Opt. Mater.* **2024**, *12*, 2302343.
[40] Y. u.-H. o. Won, O. Cho, T. Kim, D-Y. Chung, T. Kim, H. Chung, H. Jang, J. Lee, D. Kim, E. Jang, *Nature* **2019**, *575*, 634.
[41] J. Lin, S. Chen, W. Ye, Y. Zeng, H. Xiao, T. Pang, Y. Zheng, B. Zhuang, F. Huang, D. Chen, *Adv. Funct. Mater.* **2024**, *34*, 2314795.
[42] H. Li, Y. Liang, S. Liu, W. Zhang, Y. Bi, Y. Gong, W. Lei, *Adv. Opt. Mater.* **2021**, *9*, 2100799.
[43] C. Liu, Z. Zhou, Y. Zhang, *J. Lumin.* **2019**, *213*, 1.
[44] G. Chen, Y. Cao, Z. Li, X. Wang, Y. Wang, *Chem. Commun.* **2024**, *60*, 5687.
[45] C. Liu, Z. Qi, C-G. Ma, P. Dorenbos, D. Hou, S. u. Zhang, X. Kuang, J. Zhang, H. Liang, *Chem. Mater.* **2014**, *26*, 3709.
[46] Z. Yang, S. Zheng, G. Xi, T. Pang, S. Wang, Q. Ye, B. Zhuang, D. Chen, *J. Adv. Ceram.* **2023**, *12*, 2075.
[47] Y. Ma, X. Li, L. Wu, C. Shao, B. Zhang, T. Pang, L. Lu, H. Qiu, Y. e. Tian, G. Wang, Y. Hui, Q. Guo, D. Chen, *J. Adv. Ceram.* **2024**, *13*, 354.
[48] G. Kresse, J. Furthmüller, *Phys. Rev. B.* **1996**, *54*, 11169.
[49] G. Kresse, D. Joubert, *Phys. Rev. B.* **1999**, *59*, 1758.
[50] P. E. Blöchl, *Phys. Rev. B.* **1994**, *50*, 17953.